

pubs.acs.org/NanoLett Letter

# Resist-Free Lithography for Monolayer Transition Metal Dichalcogenides

Preeti K. Poddar,<sup>‡</sup> Yu Zhong,<sup>‡</sup> Andrew J. Mannix, Fauzia Mujid, Jaehyung Yu, Ce Liang, Jong-Hoon Kang, Myungjae Lee, Saien Xie, and Jiwoong Park\*



Cite This: Nano Lett. 2022, 22, 726-732



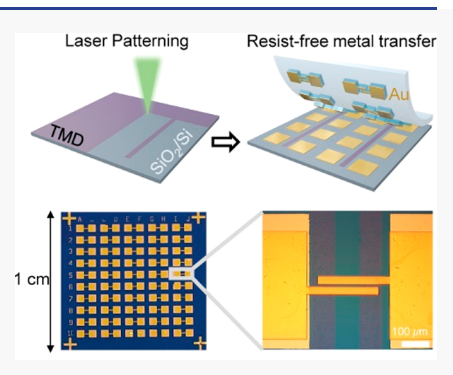
**ACCESS** 

Metrics & More

Article Recommendations

Supporting Information

**ABSTRACT:** Photolithography and electron-beam lithography are the most common methods for making nanoscale devices from semiconductors. While these methods are robust for bulk materials, they disturb the electrical properties of two-dimensional (2D) materials, which are highly sensitive to chemicals used during lithography processes. Here, we report a resist-free lithography method, based on direct laser patterning and resist-free electrode transfer, which avoids unintentional modification to the 2D materials throughout the process. We successfully fabricate large arrays of field-effect transistors using MoS<sub>2</sub> and WSe<sub>2</sub> monolayers, the performance of which reflects the properties of the pristine materials. Furthermore, using these pristine devices as a reference, we reveal that among the various stages of a conventional lithography process, exposure to a solvent like acetone changes the electrical conductivity of MoS<sub>2</sub> the most. This new approach will enable a rational design of reproducible processes for making large-scale integrated circuits based on 2D materials and other surface-sensitive materials.



KEYWORDS: Two-dimensional materials, Molybdenum disulfide, Field-effect transistors, Doping, Lithography

he electrical performance of semiconductor devices in integrated circuits is determined by both the properties of the semiconducting material (e.g., p-type vs n-type) and the effects of subsequent processes that are carried out on the material during device fabrication. The contribution from the latter becomes more significant in atomically thin materials such as transition metal dichalcogenides (TMDs) for two reasons. First, TMDs are all-surface materials in which electrical currents flow through the surface.<sup>2-4</sup> Hence, many steps in conventional lithography which are performed on the surfaces of materials (e.g., resist coating, exposure to ultraviolet light, solvent for development, and cleaning) may unintentionally modify the electrical properties of such materials. Second, TMDs are atomically thin and thus easy to damage. For example, direct evaporation of hot metals for electrical contacts is known to affect the overall electrical device conductivity. 5,6 Therefore, different electrical properties can be seen even when the same starting material is used to fabricate devices using procedures involving different chemicals and processes. This poses an important challenge: to produce devices based on monolayer TMDs with the desired properties, one needs to determine the electrical properties of the starting material, often as-grown thin films, and then understand the effects of individual device fabrication steps on those properties. However, the current lithography-based device fabrication approaches cannot provide accurate information regarding the properties of the starting materials since the lithography process itself affects the measured

outcome. Moreover, the origin of unintentional modifications to TMDs during conventional lithography has not been completely understood. This has led to the wide range of electrical characteristics of TMD-based devices.<sup>7–9</sup>

To achieve predictable and controllable performance of TMD-based devices, a new lithography method for device fabrication is needed. First, the method to define conductance channels should use a patterning approach that does not affect the surface of the material or device. Second, the process to define electrical contacts should be nonperturbative and resistfree to minimize any thermal, mechanical, and chemical damage to the device. Third, the method should be scalable to produce large-area device arrays. To date, several unconventional approaches for defining contacts have been developed, including shadow metal evaporation and electrode transfer. 5,6,10,11 However, shadow metal evaporation damages the material surface, and the current electrode transfer protocols require the resist touching the channel surface. For defining conductance channels, unconventional methods such as patterned growth and tip-based scratching have been demonstrated. 12,13 Nonetheless, there lacks a fabrication

Received: October 21, 2021 Revised: January 6, 2022 Published: January 10, 2022





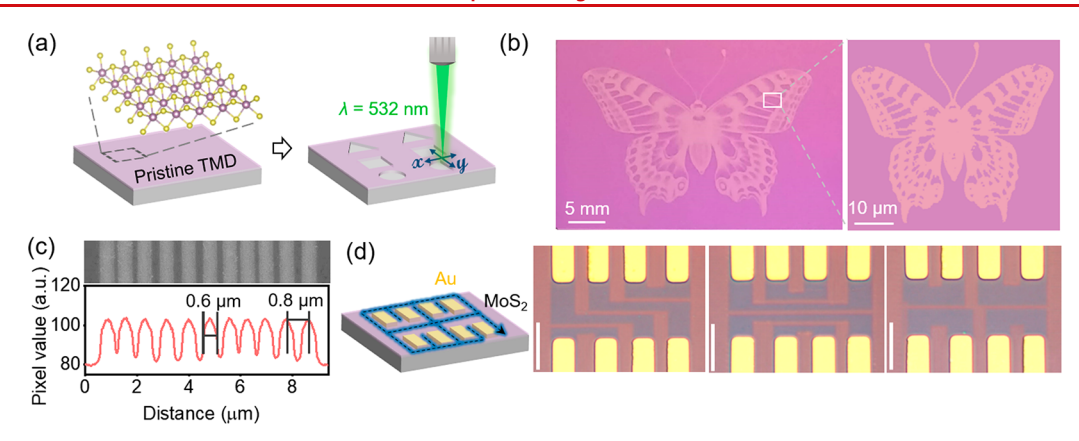


Figure 1. Scalable, high-resolution patterning of TMDs. (a) Schematic of laser-based patterning of pristine as-grown monolayer TMDs using a Q-switched 532 nm laser. (b) Photograph of large-scale patterned (left) and optical micrograph of small-scale patterned (right) monolayer  $MoS_2$ . The areas with lighter color have been laser-ablated. (c) SEM image of laser-patterned  $MoS_2$  (top) and corresponding line profiles (bottom) extracted from the image. (d) Schematic of the laser patterning of  $MoS_2$  after making electrode contacts (left) and optical images of three different designs of  $MoS_2$  channels using similar sets of eight gold electrodes (right). Scale bars are 10  $\mu$ m.

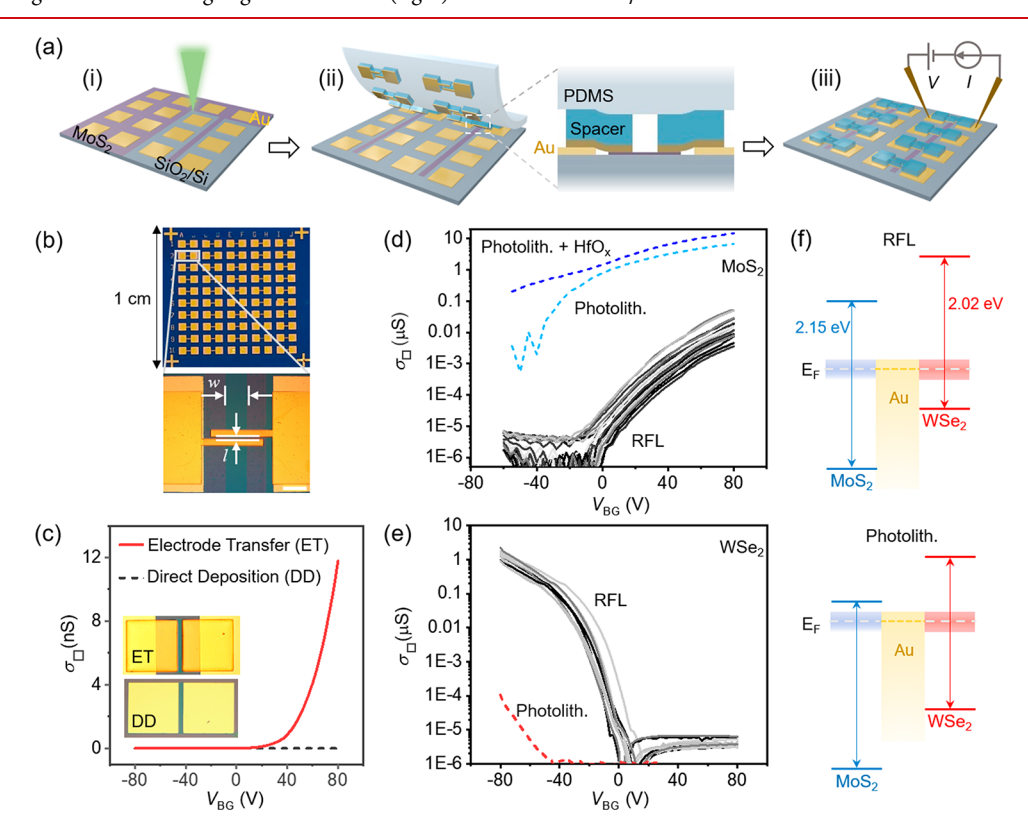


Figure 2. Resist-free lithography for monolayer TMDs. (a) Schematic illustrating the resist-free lithography process. (b) Photograph of a transferred electrode array onto MoS<sub>2</sub> channels, with magnified optical image of a transferred electrodes pair. Scale bar is 100 μm. (c) Representative transfer curves for MoS<sub>2</sub> channels, with contacts defined via electrode transfer (ET) and direct deposition (DD). Inset: Photographs of two devices fabricated using ET and DD of electrodes with the same aspect ratio. The size of the square pad is 110 × 110 μm. (d, e) Sheet conductivity vs back gate voltage for (d) MoS<sub>2</sub> and (e) WSe<sub>2</sub> devices respectively fabricated by solid lines: RFL; dashed lines: photolithography (light blue in Figure 2d and red in Figure 2e) and photolithography combined with hafnium oxide dielectric deposition (dark blue in Figure 2d). (f) Band alignments of MoS<sub>2</sub> (or WSe<sub>2</sub>) and gold (work function ~5.1 eV)<sup>5</sup> expected for RFL (top) and after photolithography (bottom).  $E_F$  is the Fermi level of the system. The energy levels are drawn considering free-particle band gaps of MoS<sub>2</sub> and WSe<sub>2</sub>.<sup>36</sup>

method that provides all of the needed capabilities described above.

Here, we report a resist-free lithography (RFL) process for fabrication of field-effect transistors (FETs) based on atomically thin materials with the aforementioned characteristics. This method is based on a laser-patterning technique that directly defines conductance channels, while keeping the surface pristine, and a resist-free transfer of premade metal

electrodes that minimizes damage to the material. Both processes can be carried out over a large scale. When applied to wafer-scale materials, this method allows for the batch fabrication of many devices for statistical analysis. We use this method to measure the pristine properties of large-scale MoS<sub>2</sub> and WSe<sub>2</sub> monolayers, as-grown by metal—organic chemical vapor deposition. Both MoS<sub>2</sub> and WSe<sub>2</sub> FETs exhibit transistor behaviors as predicted from their pristine forms

Nano Letters pubs.acs.org/NanoLett Letter

and band alignments. Furthermore, RFL enables us to study the unintentional doping of these materials during conventional lithography processes which has yet been inaccessible by other methods. We monitor the evolution of electrical properties along typical lithography processes and find that exposure to acetone solvent increases the conductivity of MoS<sub>2</sub> the most, while the deposition of resists has surprisingly negligible effects. We further conduct systematic measurements to show that exposure to different solvents leads to different on-state conductance of MoS<sub>2</sub>, an effect that can be explained by a solvent-induced doping effect using their electronegativities.

Figure 1 and Figure 2 describe the two key features of our RFL approach: the direct laser patterning (illustrated in Figure 1a) and the resist-free transfer of electrodes (Figure 2a). The laser patterning is conducted by raster scanning a focused laser beam (532 nm Q-switched pulsed laser) with controlled power and position to selectively remove the exposed film areas. The removal is mainly caused by the absorption of the laser leading to thermal ablation, <sup>15</sup> and this process ensures that the untouched areas of the TMD films remain unaffected (Figure S1). Similarly, this technique is effective for patterning other light-absorbing materials, such as metal thin films (Figure S2). We note that the power of the laser needs to be carefully optimized on the basis of a power-dependent assay (Figure S3) to selectively pattern each material without damaging the underlying substrate (for example, SiO<sub>2</sub>/Si in our experiment).

Figure 1b shows two examples of monolayer MoS<sub>2</sub> on SiO<sub>2</sub>/ Si, each patterned following the same butterfly design over two different length scales (left: 1 in., right: 50  $\mu$ m). This demonstrates that, depending on the choice of optical elements and magnification, the laser patterning can enable wafer-scale processing, as demonstrated for a 2-in. wafer (Figure S4), and can produce microscopic structures with a diffraction-limited spatial resolution. Figures S4e and 1c study the spatial resolution of the laser patterning, where multiple lines were drawn with varying spacings. The extracted line profile shows a minimum line width of  $\sim 0.6 \mu m$  and a minimum resolvable line pitch of  $\sim 0.8 \ \mu m$  (Figure 1c). The laser patterning can be done before or after the electrode contacts. Performing the laser patterning in the presence of electrodes provides the flexibility of defining different microscopic conductance channels between similar sets of metal electrodes as shown in Figure 1d.

Figure 2a explains the resist-free electrode transfer of metal contacts and how this is used for measuring the pristine electrical properties of TMDs. To do this, (i) we start with an as-grown wafer-scale MoS2 monolayer film with an array of large metal pads (deposited via shadow evaporation), which are used for probing only. The MoS<sub>2</sub> is then patterned using the laser to make conductive channels aligned to the metal pads. (ii) To make the actual electrical contacts to MoS<sub>2</sub>, gold electrode/polymer spacer bilayers are fabricated on a separate substrate by photolithography and transferred onto the MoS<sub>2</sub> film using a polydimethylsiloxane (PDMS) stamp. The purpose of the polymer spacers (1-10  $\mu$ m thick) on top of the gold electrodes is to avoid direct contact between the PDMS and the surface of the MoS<sub>2</sub> (see the schematic of the cross-section in Figure 2a (ii) and optical images in Figure S5). Release of the PDMS stamp by gentle heating completes our electrode transfer and the FET device fabrication process. The devices are measured under ambient conditions on a probe station using Si substrate as a back gate (iii). Figure 2b shows

an optical image of a completed electrode array made using this process over a centimeter length scale (top) and a magnified image of a pair of transferred electrodes (bottom; with transparent spacer layers). We note that the channel width (w) is defined by the laser patterning and the channel length (l) by the transferred electrode design. The precision of this fabrication method is about  $\pm 5~\mu m$ , which is limited by alignment accuracy for the electrode transfer process. With a better transfer stage, this method can be used for making more complex and smaller devices. The details of the entire process are included in the Methods section (see Supporting Information).

The electrodes transferred in this way make better electrical contacts to the  $MoS_2$  as shown in Figure 2c. For this comparison, two sets of  $MoS_2$  channels with the same dimensions ( $l \sim 11~\mu m$  and  $w \sim 117~\mu m$ ) are made using the laser patterning method. The only difference between them is how the contacts are made; for one, the gold contacts are defined using our resist-free electrode transfer, while for the other direct contact, shadow evaporation is used. Only the devices made with transferred electrodes turn on at positive backgate voltage ( $V_{\rm BG}$ ), showing finite sheet conductivity ( $\sigma_{\square}$ ). The result confirms that our transferred electrodes result in lower contact resistances compared with those of directly deposited ones. This is because the transferred electrodes do not damage TMDs (Figure S6), while direct deposition does. S6

We now use the RFL method to study the electrical conductivities of pristine, as-grown monolayer MoS2 and WSe<sub>2</sub>. Figure 2d plots  $\sigma_{\square}$ - $V_{\rm BG}$  curves measured from an array of 20 MoS<sub>2</sub> FETs with the same dimensions as shown in Figure 2b, all of which show similar behaviors. The measured  $\sigma_{\square}$  is very low (<10<sup>-5</sup> $\mu$ S) for negative  $V_{\rm BG}$  and increases for positive  $V_{\rm BG}$  by approximately 4 orders of magnitude, reaching around 0.01  $\mu$ S at  $V_{BG}$  = 80 V. The curves show an exponential  $V_{\rm BG}$ -dependence near  $V_{\rm BG} = 0$  V, which suggests that they are in the subthreshold regime. For comparison, a  $\sigma_{\square} {-} V_{\rm BG}$  curve (light blue dashed line) measured from a similarly grown MoS<sub>2</sub> film is shown, where the electrodes and channels are fabricated using conventional photolithography and direct deposition. It shows a much higher  $\sigma_{\square}$  (more than 100 times higher) and a linear  $V_{\rm BG}$ -dependence, in contrast to the results of pristine  $MoS_2$  film.  $\sigma_{\square}$  increases further after the deposition of a hafnium oxide dielectric on the surface (dark blue dashed line), and measurements from multiple such devices yield a high electron mobility (21  $\pm$  4 cm<sup>2</sup>/V·s). Figure 2e shows a similar comparison conducted using monolayer WSe2. The WSe2 FETs fabricated using RFL exhibit high  $\sigma_{\square}$  at negative  $V_{\text{BG}}$ that decreases with increasing  $V_{\rm BG}$ . The devices show a hole mobility of  $4 \pm 1$  cm<sup>2</sup>/V·s, a threshold voltage of  $-53 \pm 2$  V, and an on-off ratio of  $\sim 10^6$  as measured from multiple devices. In contrast, the devices fabricated via a conventional photolithography-based approach show a drastically different response (red dashed line), exhibiting much lower conductivity.

The data in Figure 2d,e clearly illustrate that significant differences occur in the measured conductivities of monolayer TMDs when different device fabrication approaches are used. It also explains how such comparisons can be used to monitor the properties of TMDs starting from the growth and during a device fabrication process. First, our RFL method allows us to probe their properties as grown, providing reference points. Our data in Figure 2d,e suggest that the MoS<sub>2</sub> channels exhibit

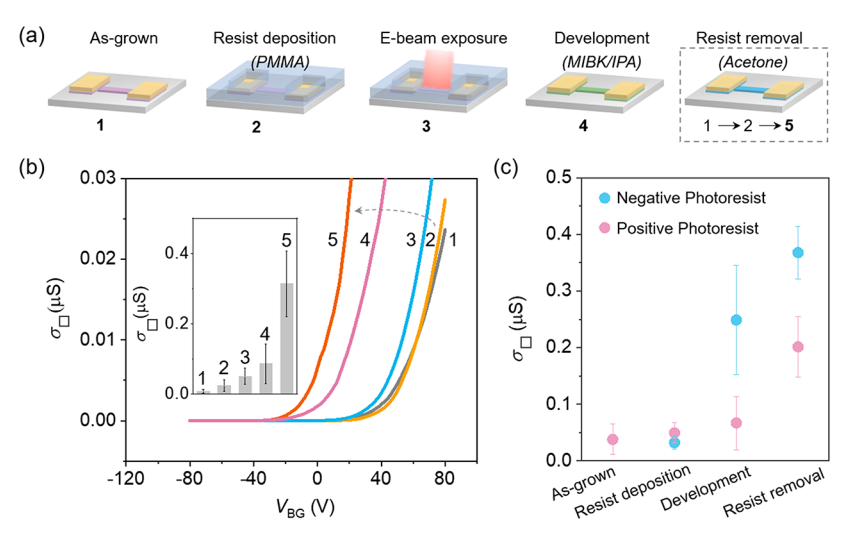


**Figure 3.** Unintentional doping during conventional lithography. (a) Schematic of MoS<sub>2</sub> channels at different fabrication steps involved in EBL. (b) Representative transfer curves of as-grown MoS<sub>2</sub> and ones obtained at numerically designated process steps in Figure 3a of EBL. Inset: Mean on-state conductivity from 15 devices at each step. (c) Mean on-state conductivity (each from 11 devices) of MoS<sub>2</sub> channels during different processing steps of photolithography, plotted for two different photoresists.

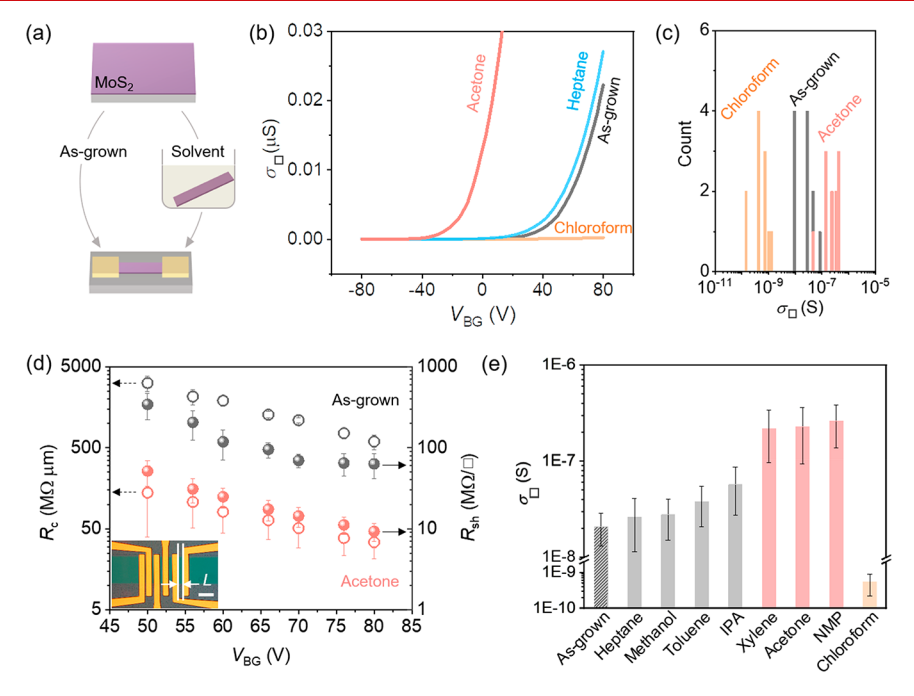


Figure 4. Effect of organic solvents on  $MoS_2$  conductivity. (a) Schematic of experimental pathway to study the solvent effects. (b) Representative transfer curves of as-grown  $MoS_2$  and ones obtained after exposure of channels to acetone, chloroform and heptane. (c) Histograms of on-state conductivities at  $V_{BG} = 80$  V corresponding to the channels shown in Figure 4b. (d) Contact and sheet resistance for as-grown and acetone-exposed  $MoS_2$  measured using the transfer length technique. Inset: Optical micrograph device used for channel length measurements, where channel length, L is denoted. Scale bar is  $50 \ \mu m$ . (e) Mean on-state conductivities (each from 11 devices) for  $MoS_2$  channels as-grown and treated with different organic solvents.

lightly doped, n-type conductivities, while the WSe $_2$  channels show a p-type behavior. This is consistent with the expected band alignments between MoS $_2$  (or WSe $_2$ ) and gold (see Figure 2f, top). Second, comparing these results with that of devices made using conventional-lithography shows the net effect of the processes used for the device fabrication. In our experiment, the particular photolithography process leads to a further n-type doping of the TMD channels, increasing  $\sigma_{\square}$  of MoS $_2$ , which is n-type as-grown, and decreasing  $\sigma_{\square}$  of WSe $_2$ , which is p-type (see Figure 2f, bottom).

The changes of  $\sigma_{\square}$  observed in Figure 2 after the photolithography are a result of the combined effects of many steps applied to the as-grown TMD monolayers. Our RFL method can be used to resolve the effect of individual fabrication steps, including, for example, resist coating, exposure, development, and resist removal. In Figure 3, we demonstrate this by measuring the changes in  $\sigma_{\square}$  after each step during an example electron beam lithography (EBL) process. Figure 3a shows a schematic of MoS<sub>2</sub> channels at various processing steps of EBL, whose conductivity is measured and compared to that of unprocessed, as-grown

MoS $_2$  channel, fabricated using RFL (1), which acts as a reference. The EBL process involves poly methyl methacrylate (PMMA) resist deposition (2), e-beam exposure (3), and development in methyl isobutyl ketone in isopropanol (MIBK/IPA) (4). We measure the  $\sigma_{\square}$ – $V_{\rm BG}$  curves after each step. In addition, we measure the effect of acetone-based removal of PMMA (1 $\rightarrow$ 2 $\rightarrow$ 5) without exposure to e-beam and a developer solution. Slightly different experimental procedures are used for each checkpoint to perform the measurements. For example, steps (2) and (3) involve transfer of a layer of PMMA on MoS $_2$  channel to improve the device yield. We note that transferred PMMA and spin-coated PMMA show a similar effect on the conductivity of the MoS $_2$  channels (Figure S7). These experimental details are explained in the Methods section (Supporting Information).

Figure 3b shows representative  $\sigma_{\square} - V_{\text{BG}}$  curves measured at these checkpoints. The curves shift progressively toward more negative gate voltages going from (1) to (5), where the magnitude of the shift,  $\Delta V_{\mathrm{BG}}$  (measured with respect to curve 1) varies for each step.  $\Delta V_{\rm BG}$  is small after the deposition of PMMA (2) and an e-beam exposure (3). There are considerable increases in  $\Delta V_{\rm BG}$  after the development (4) by ~40 V and after an acetone-based PMMA removal (5) by ~60 V. The inset in Figure 3b plots the average  $\sigma_{\square}$  measured at  $V_{\text{BG}}$ = 80 V (each based on results from 15 devices) and shows an increasing  $\sigma_{\square}$  from (1) to (5). The increase in  $\sigma_{\square}$  at a positive  $V_{\rm BG}$  and the negative shift of the  $\sigma_{\Box}$ - $V_{\rm BG}$  curves, both suggest that each step during the EBL induces further *n*-type doping. In particular, our data suggests that the doping effects from the steps that involve the exposure to solvents (MIBK/IPA developer in (4) and acetone in (5)) are larger than those from other steps. Based on the  $\Delta V_{\mathrm{BG}}$  values in Figure 3b, we estimate the increase in the carrier concentration  $(\Delta n_{\mathrm{2D}})$  in MoS<sub>2</sub> to be  $\sim 3 \times 10^{12}$  cm<sup>-2</sup> after (4) and  $\sim 4 \times 10^{12}$  cm<sup>-2</sup> after (5) based on the lateral  $\Delta V_{\rm BG}$  shifts of the transfer curves, using the parallel-plate capacitor model.<sup>16</sup> In Figure 3c, we carry out a similar set of studies for a typical photolithography process using different resists (positive and negative). The mean  $\sigma_{\square}$  measured at  $V_{\rm BG}$  = 80  $\bar{\rm V}$  from multiple channels after different process steps are shown. The results are similar to the EBL results.  $\sigma_{\square}$  remains low after the resist deposition but it increases significantly, both, after development (using a waterbased developer) and resist removal (using acetone). This leads to a surprising conclusion: an exposure to e-beam or photoresists causes relatively small changes to  $\sigma_{\square}$ , whereas the steps that remove them using solvents (a developer or acetone) result in much larger changes. This is different from a widely cited cause for the process-induced doping in TMDs and graphene, which was thought to be due to the resists. 17-24

This conclusion also suggests that exposure to liquid solvents directly affects  $\sigma_{\square}$  of TMD channels, the degree of which may vary for each solvent. This is indeed what we observe in our experiments shown in Figure 4. We investigated the effects of commonly used organic solvents on  $\sigma_{\square}$  of MoS<sub>2</sub> using our RFL method. For this, two sets of MoS<sub>2</sub> FETs are fabricated using RFL; one is based on the as-grown MoS<sub>2</sub> (to be used as a reference), and the other is based on MoS<sub>2</sub> immersed in a specific solvent overnight (see the schematic in Figure 4a). Figure 4b shows representative  $\sigma_{\square} - V_{\text{BG}}$  curves measured after acetone, heptane, and chloroform exposure alongside a curve from as-grown MoS<sub>2</sub>. The plot shows different effects from each of the three solvents. First, exposure

to heptane does not significantly change  $\sigma_{\square}$  of MoS<sub>2</sub>, in contrast to the other two. Second, while acetone shifts the  $\sigma_{\square}$  $V_{\rm BG}$  curve in the negative  $V_{\rm BG}$  direction ( $\Delta V_{\rm BG} \sim 70$  V) significantly increasing  $\sigma_{\square}$  at  $V_{BG}$  = 80 V, the MoS<sub>2</sub> does not show any measurable conductance after being exposed to chloroform. This behavior is consistently observed from many devices, as shown in the histogram in Figure 4c. Overall, these data suggest that acetone induces further n-type doping of MoS<sub>2</sub>, while chloroform has an opposite effect. This effect remains after thermal annealing at up to 200 °C (see Figure S8). This indicates that the doping effect is likely due to chemical adsorption of solvent molecules. The additional ndoping after acetone exposure also results in the increase in the overall conductivity as well as the lowering of the contact resistance. We further extract the values of the contact  $(R_c)$ and sheet resistance  $(R_{sh})$  of MoS<sub>2</sub> channels (as grown vs after acetone exposure) using RFL based on the transfer length technique  $^{25-27}$  as shown in Figure 4d.  $R_{\rm c}$  and  $R_{\rm sh}$  both become lower after acetone exposure by 1-2 orders of magnitude compared with those of the as-grown channels. In particular, the lower  $R_c$  of acetone-exposed MoS<sub>2</sub> is consistent with the ndoping effect of acetone, as it lowers the width of the Schottky barrier at the contact. This suggests that direct exposure to various solvents could be useful for systematically tuning the electrical properties of TMDs.

Figure 4e compares  $\sigma_{\square}$  of MoS<sub>2</sub> at  $V_{BG}$  = 80 V (each averaged from 11 devices) after exposure to 8 different organic solvents. There are roughly three categories of behaviors. The first set comprises heptane, toluene, methanol, and isopropyl alcohol, all of which cause minimal change to the MoS<sub>2</sub> conductivity. The second set of solvents (xylene, acetone, and n-methyl-2-pyrrolidone (NMP)) increases the conductivity by roughly an order of magnitude. The final one is chloroform which lowers the conductivity. One parameter that may explain the different doping effect by a solvent is its electronegativity ( $\chi$ ) as previously cited;<sup>28</sup> a difference in  $\chi$ generally leads to charge transfer from the system with lower  $\chi$ to the one with higher  $\chi$ . Comparing the available values of  $\chi$ for MoS<sub>2</sub> (~5.1 eV) and several solvents (see Table S1) suggests that solvents with a smaller  $\chi$  lead to further n-doping (acetone  $\sim$ 4.1 eV, xylene  $\sim$ 3.6 eV), chloroform with a higher  $\chi$ ( $\sim$ 5.5 eV) leads to the opposite effect, and heptane with  $\chi$  ( $\sim$ 5 eV) similar to MoS<sub>2</sub> causes little change. However, this correlation is not universal; for example, toluene with  $\chi \sim 3.8$ eV does not lead to *n*-doping. Indeed, the interactions between monolayer films and solvent molecules are complex and influenced by other factors (e.g., charge rearrangement, molecular orientation, etc.) as discussed in other studies.<sup>29,30</sup> The doping mechanism could include chemical reaction, surface adsorption, and charge transfer from solvent molecules. The RFL method thus provides precise information, separate from the effects of conventional lithography, and therefore could allow the careful study of such molecule-TMD interactions for various solvent molecules and 2D materials in the future.

In conclusion, we have developed a scalable, RFL method to fabricate devices on the basis of pristine monolayers of TMDs with predictable performances and measured the unintentional doping caused during the conventional lithography. The lithography processes in our experiments n-dope the TMDs, leading to an increase (decrease) in the conductivity of  $MoS_2$  (WSe<sub>2</sub>). We employ RFL to resolve the effects from individual steps of lithography and find that common solvents introduce

Nano Letters pubs.acs.org/NanoLett Letter

different doping effects. This method offers a much-needed platform for device fabrication applicable to various surface-sensitive 2D layered materials. It can be used during the testing and development of processes for controlling their electrical properties, including atomic substitution<sup>31,32</sup> and surface functionalization.<sup>33,34</sup> Devices made using RFL could provide highly sensitive and reproducible chemical sensors<sup>35</sup> based on TMDs with low doping levels. Our versatile RFL method, therefore, equips us with the ability to precisely design and control the performance of next-generation TMD-based optoelectronic devices and circuits.

## ASSOCIATED CONTENT

# **Supporting Information**

The Supporting Information is available free of charge at https://pubs.acs.org/doi/10.1021/acs.nanolett.1c04081.

Methods; characterization of laser patterned MoS<sub>2</sub>; laser patterning of metal films; optimization of patterning parameters for selective etching of MoS<sub>2</sub>; flexibility in scale and resolution of patterning; preservation of asgrown channel surface during electrode transfer; effect of thermal annealing on MoS<sub>2</sub> conductivity after acetone exposure; table of electronegativity values for solvent and MoS<sub>2</sub> (PDF)

## AUTHOR INFORMATION

## **Corresponding Author**

Jiwoong Park — Department of Chemistry, University of Chicago, Chicago, Illinois 60637, United States; James Franck Institute and Pritzker School of Molecular Engineering, University of Chicago, Chicago, Illinois 60637, United States; Email: jwpark@uchicago.edu

# Authors

Preeti K. Poddar — Department of Chemistry, University of Chicago, Chicago, Illinois 60637, United States;
o orcid.org/0000-0002-1594-2709

Yu Zhong – Department of Chemistry, University of Chicago, Chicago, Illinois 60637, United States

Andrew J. Mannix – James Franck Institute, University of Chicago, Chicago, Illinois 60637, United States;
orcid.org/0000-0003-4788-1506

Fauzia Mujid – Department of Chemistry, University of Chicago, Chicago, Illinois 60637, United States

**Jaehyung Yu** – Department of Chemistry, University of Chicago, Chicago, Illinois 60637, United States

Ce Liang – Pritzker School of Molecular Engineering, University of Chicago, Chicago, Illinois 60637, United States

Jong-Hoon Kang — Department of Chemistry, University of Chicago, Chicago, Illinois 60637, United States;
orcid.org/0000-0002-5109-8402

Myungjae Lee – James Franck Institute, University of Chicago, Chicago, Illinois 60637, United States

Saien Xie — Pritzker School of Molecular Engineering, University of Chicago, Chicago, Illinois 60637, United States

Complete contact information is available at: https://pubs.acs.org/10.1021/acs.nanolett.1c04081

## **Author Contributions**

<sup>‡</sup>P.K.P. and Y.Z. contributed equally to this work.

#### Notes

The authors declare no competing financial interest.

### ACKNOWLEDGMENTS

Primary funding for this work comes from Samsung Advanced Institute of Technology and Air Force Office of Scientific Research (FA9550-16-1-0347, FA9550-21-1-0323, MURI project; FA9550-18-1-0480). Additional funding was provided by the University of Chicago MRSEC (NSF DMR-2011854), the Cornell Center for Materials Research (NSF DMR-1719875), and the Center for Novel Pathways to Quantum Coherence in Materials, an Energy Frontier Research Center funded by the U.S. Department of Energy. F.M. acknowledges support by the NSF Graduate Research Fellowship Program under Grant No. DGE-1746045. This work makes use of the fabrication facilities of the Pritzker Nanofabrication Facility at the University of Chicago, which receives support from SHyNE Resource (NSF ECCS-420 1542205), a node of NSF's NNCI network and Searle Cleanroom and Nanofabrication Facility at the University of Chicago. Y.Z. acknowledges support by the Camille and Henry Dreyfus Foundation, Inc., under the Dreyfus Environmental Postdoc award EP-16-094.

## REFERENCES

- (1) Campbell, S. A. Fabrication engineering at the micro- and nanoscale; Oxford University Press, 2008; pp 3–9.
- (2) Wang, Q. H.; Kalantar-Zadeh, K.; Kis, A.; Coleman, J. N.; Strano, M. S. Electronics and optoelectronics of two-dimensional transition metal dichalcogenides. *Nat. Nanotechnol.* **2012**, *7*, 699–712.
- (3) Lin, Z.; McCreary, A.; Briggs, N.; Subramanian, S.; Zhang, K.; Sun, Y.; Li, X.; Borys, N. J.; Yuan, H.; Fullerton-Shirey, S. K.; Chernikov, A.; Zhao, H.; McDonnell, S.; Lindenberg, A. M.; Xiao, K.; LeRoy, B. J.; Drndić, M.; Hwang, J. C. M.; Park, J.; Chhowalla, M.; et al. 2D materials advances: from large scale synthesis and controlled heterostructures to improved characterization techniques, defects and applications. 2D Mater. 2016, 3, 042001.
- (4) Rhodes, D.; Chae, S. H.; Ribeiro-Palau, R.; Hone, J. Disorder in van der Waals heterostructures of 2D materials. *Nat. Mater.* **2019**, *18*, 541–549.
- (5) Liu, Y.; Guo, J.; Zhu, E.; Liao, L.; Lee, S.-J.; Ding, M.; Shakir, I.; Gambin, V.; Huang, Y.; Duan, X. Approaching the Schottky-Mott limit in van der Waals metal-semiconductor junctions. *Nature* **2018**, 557, 696–700.
- (6) Kong, L.; Zhang, X.; Tao, Q.; Zhang, M.; Dang, W.; Li, Z.; Feng, L.; Liao, L.; Duan, X.; Liu, Y. Doping-free complementary WSe<sub>2</sub> circuit via van der Waals metal integration. *Nat. Commun.* **2020**, *11*, 1–7.
- (7) Fiori, G.; Bonaccorso, F.; Iannaccone, G.; Palacios, T.; Neumaier, D.; Seabaugh, A.; Banerjee, S. K.; Colombo, L. Electronics based on two-dimensional materials. *Nat. Nanotechnol.* **2014**, *9*, 768–779.
- (8) Schwierz, F.; Pezoldt, J.; Granzner, R. Two-dimensional materials and their prospects in transistor electronics. *Nanoscale* **2015**, 7, 8261–8283.
- (9) Sebastian, A.; Pendurthi, R.; Choudhury, T. H.; Redwing, J. M.; Das, S. Benchmarking monolayer MoS<sub>2</sub> and WS<sub>2</sub> field-effect transistors. *Nat. Commun.* **2021**, *12*, 693.
- (10) Park, W.; Baik, J.; Kim, T.-Y.; Cho, K.; Hong, W.-K.; Shin, H.-J.; Lee, T. Photoelectron spectroscopic imaging and device applications of large-area patternable single-layer MoS<sub>2</sub> synthesized by chemical vapor deposition. *ACS Nano* **2014**, *8*, 4961–4968.
- (11) Telford, E. J.; Benyamini, A.; Rhodes, D.; Wang, D.; Jung, Y.; Zangiabadi, A.; Watanabe, K.; Taniguchi, T.; Jia, S.; Barmak, K.; Pasupathy, A. N.; Dean, C. R.; Hone, J. Via Method for Lithography Free Contact and Preservation of 2D Materials. *Nano Lett.* **2018**, *18*, 1416–1420.
- (12) Guo, Y.; Shen, P.-C.; Su, C.; Lu, A.-Y.; Hempel, M.; Han, Y.; Ji, Q.; Lin, Y.; Shi, E.; McVay, E.; Dou, L.; Muller, D. A.; Palacios, T.; Li,

- J.; Ling, X.; Kong, J. Additive manufacturing of patterned 2D semiconductor through recyclable masked growth. *Proc. Natl. Acad. Sci. U. S. A.* **2019**, *116*, 3437–3442.
- (13) Wei, Z.; Liao, M.; Guo, Y.; Tang, J.; Cai, Y.; Chen, H.; Wang, Q.; Jia, Q.; Lu, Y.; Zhao, Y.; Liu, J.; Chu, Y.; Yu, H.; Li, N.; Yuan, J.; Huang, B.; Shen, C.; Yang, R.; Shi, D.; Zhang, G. Scratching lithography for wafer-scale MoS<sub>2</sub> monolayers. 2D Mater. 2020, 7, 045028.
- (14) Kang, K.; Xie, S.; Huang, L.; Han, Y.; Huang, P. Y.; Mak, K. F.; Kim, C.-J.; Muller, D.; Park, J. High-mobility three-atom-thick semiconducting films with wafer-scale homogeneity. *Nature* **2015**, *520*, *656*–*660*.
- (15) Castellanos-Gomez, A.; Barkelid, M.; Goossens, A. M.; Calado, V. E.; van der Zant, H. S. J.; Steele, G. A. Laser-thinning of MoS<sub>2</sub>: On demand generation of a single-layer semiconductor. *Nano Lett.* **2012**, 12, 3187–3192.
- (16) Radisavljevic, B.; Kis, A. Mobility engineering and a metal-insulator transition in monolayer MoS<sub>2</sub>. *Nat. Mater.* **2013**, *12*, 815–820.
- (17) Liang, J.; Xu, K.; Toncini, B.; Bersch, B.; Jariwala, B.; Lin, Y.-C.; Robinson, J.; Fullerton-Shirey, S. K. Impact of post-lithography polymer residue on the electrical characteristics of MoS<sub>2</sub> and WSe<sub>2</sub> field effect transistors. *Adv. Mater. Interfaces* **2019**, *6*, 1801321.
- (18) Suk, J. W.; Lee, W. H.; Lee, J.; Chou, H.; Piner, R. D.; Hao, Y.; Akinwande, D.; Ruoff, R. S. Enhancement of the electrical properties of graphene grown by chemical vapor deposition via controlling the effects of polymer residue. *Nano Lett.* **2013**, *13*, 1462–1467.
- (19) Lin, Y.-C.; Lu, C.-C.; Yeh, C.-H.; Jin, C.; Suenaga, K.; Chiu, P.-W. Graphene annealing: how clean can it be? *Nano Lett.* **2012**, *12*, 414–419.
- (20) Pirkle, A.; Chan, J.; Venugopal, A.; Hinojos, D.; Magnuson, C. W.; McDonnell, S.; Colombo, L.; Vogel, E. M.; Ruoff, R. S.; Wallace, R. M. The effect of chemical residues on the physical and electrical properties of chemical vapor deposited graphene transferred to SiO<sub>2</sub>. *Appl. Phys. Lett.* **2011**, *99*, 122108.
- (21) Ahn, Y.; Kim, H.; Kim, Y.-H.; Yi, Y.; Kim, S.-Il. Procedure of removing polymer residues and its influences on electronic and structural characteristics of graphene. *Appl. Phys. Lett.* **2013**, *102*, 091602.
- (22) Dan, Y.; Lu, Y.; Kybert, N. J.; Luo, Z.; Johnson, A. T. C. Intrinsic response of graphene vapor sensors. *Nano Lett.* **2009**, *9*, 1472–1475.
- (23) Moser, J.; Barreiro, A.; Bachtold, A. Current-induced cleaning of graphene. *Appl. Phys. Lett.* **2007**, *91*, 163513.
- (24) Jia, Y.; Gong, X.; Peng, P.; Wang, Z.; Tian, Z.; Ren, L.; Fu, Y.; Zhang, H. Toward high carrier mobility and low contact resistance: laser cleaning of PMMA residues on graphene surfaces. *Nano-Micro Lett.* **2016**, *8*, 336–346.
- (25) Guimarães, M. H. D.; Gao, H.; Han, Y.; Kang, K.; Xie, S.; Kim, C.-J.; Muller, D. A.; Ralph, D. C.; Park, J. Atomically thin ohmic edge contacts between two-dimensional materials. *ACS Nano* **2016**, *10*, 6392–6399.
- (26) Liu, H.; Neal, A. T.; Ye, P. D. Channel length scaling of MoS<sub>2</sub> MOSFETs. ACS Nano 2012, 6, 8563–8569.
- (27) Liu, H.; Si, M.; Deng, Y.; Neal, A. T.; Du, Y.; Najmaei, S.; Ajayan, P. M.; Lou, J.; Ye, P. D. Switching mechanism in single-layer molybdenum disulfide transistors: An insight into current flow across Schottky barriers. *ACS Nano* **2014**, *8*, 1031–1038.
- (28) Choi, J.; Zhang, H.; Du, H.; Choi, J. H. Understanding solvent effects on the properties of two-dimensional transition metal dichalcogenides. ACS Appl. Mater. Interfaces 2016, 8, 8864–8869.
- (29) Patil, U.; Caffrey, N. M. Adsorption of common solvent molecules on graphene and MoS<sub>2</sub> from first-principles. *J. Chem. Phys.* **2018**, *149*, 094702.
- (30) Roychoudhury, S.; Motta, C.; Sanvito, S. Charge transfer energies of benzene physisorbed on a graphene sheet from constrained density functional theory. *Phys. Rev. B* **2016**, *93*, 1–8.
- (31) Gao, H.; Suh, J.; Cao, M. C.; Joe, A. Y.; Mujid, F.; Lee, K.-H.; Xie, S.; Poddar, P.; Lee, J.-U.; Kang, K.; Kim, P.; Muller, D. A.; Park, J.

- Tuning electrical conductance of MoS<sub>2</sub> monolayers through substitutional doping. *Nano Lett.* **2020**, *20*, 4095–4101.
- (32) Guo, Y.; Lin, Y.; Xie, K.; Yuan, B.; Zhu, J.; Shen, P.-C.; Lu, A.-Y.; Su, C.; Shi, E.; Zhang, K.; HuangFu, C.; Xu, H.; Cai, Z.; Park, J.-H.; Ji, Q.; Wang, J.; Dai, X.; Tian, X.; Huang, S.; Dou, L.; et al. Designing artificial two-dimensional landscapes via atomic-layer substitution. *Proc. Natl. Acad. Sci. U. S. A.* **2021**, *118*, No. e2106124118.
- (33) Mouri, S.; Miyauchi, Y.; Matsuda, K. Tunable photoluminescence of monolayer  $MoS_2$  via chemical doping. *Nano Lett.* **2013**, *13*, 5944–5948.
- (34) Pak, S.; Jang, A.-R.; Lee, J.; Hong, J.; Giraud, P.; Lee, S.; Cho, Y.; An, G.-H.; Lee, Y.-W.; Shin, H. S.; Morris, S. M.; Cha, S.; Sohn, J. I.; Kim, J. M. Surface functionalization-induced photoresponse characteristics of monolayer MoS<sub>2</sub> for fast flexible photodetectors. *Nanoscale* **2019**, *11*, 4726–4734.
- (35) Perkins, F. K.; Friedman, A. L.; Cobas, E.; Campbell, P. M.; Jernigan, G. G.; Jonker, B. T. Chemical vapor sensing with monolayer MoS<sub>2</sub>. *Nano Lett.* **2013**, *13*, 668–673.
- (36) Wang, G.; Chernikov, A.; Glazov, M. M.; Heinz, T. F.; Marie, X.; Amand, T.; Urbaszek, B. Colloquium: Excitons in atomically thin transition metal dichalcogenides. *Rev. Mod. Phys.* **2018**, *90*, 1–25.

